Research Square

Preprints are preliminary reports that have not undergone peer review.
They should not be considered conclusive, used to inform clinical practice,
or referenced by the media as validated information.

Dynamics of a bioinspired feathered flapping wing including contact modeling

Renan Cavenaghi Silva

cavenaghi.silva@unesp.br

São Paulo State University

Daniel García-Vallejo

University of Seville

Douglas D. Bueno

São Paulo State University

Research Article

Keywords: Feathered Flapping Wing, Absolute nodal coordinate formulation, Dynamics, Contact model

Posted Date: June 4th, 2026

DOI: https://doi.org/10.21203/rs.3.rs-9884899/v1

License: This work is licensed under a Creative Commons Attribution 4.0 International License.
Read Full License

Additional Declarations: No competing interests reported.

Dynamics of a bioinspired feathered flapping wing including contact modeling

Renan Cavenaghi Silva[*], **Daniel García-Vallejo**[#], **Douglas D. Bueno**[*]

[*] Department of Mechanical Engineering
São Paulo State University (UNESP)
School of Engineering, Ilha Solteira
Av. Brasil Sul, 56 - Centro, 15385-007, Ilha Solteira Brazil
[cavenaghi.silva, douglas.bueno]@unesp.br
[#] Department of Mechanical and Manufacturing Engineering
University of Seville
Escuela Técnica Superior de Ingeniería de Sevilla
Camino de los descubrimientos S/N, 41092, Seville, Spain
dgvallejo@us.es

ABSTRACT

Birds evolved to have wings made of several feathers with an overlap between adjacent vanes. This assembly configuration enables them to deform relatively independently during the flapping cycle. However, due to the overlap, this dependence only occurs during part of the cycle, as the contact on the overlapping regions couples their deformation. In this work, a line-to-line continuous-contact formulation is implemented to model bioinspired wings composed of several flexible airfoils that are positioned along a rigid wing with an overlap. The airfoil structure is represented by three-dimensional beam elements based on absolute nodal coordinate formulation (ANCF). Then, the constraint equation responsible for the imposition of the flapping motion and the resulting equation of motion are numerically integrated using the generalized-α algorithm to investigate how the gap varies during the flapping cycle and the effect of contact parameters on the airfoils dynamic response.

Keywords: Feathered Flapping Wing · Absolute nodal coordinate formulation · Dynamics · Contact model

1 INTRODUCTION

Natural selection is Nature's mechanism of optimization that refines the traits that improve survivability for the species. This process has been ongoing for millions of years, and eventually it resulted in the development by some species of three distinct evolutionary branches the ability to fly. Birds are the class most recognized by their biodiversity of species specializing in different skills (e.g., maneuverability, stealth, speed, strength, endurance), with several morphological adaptations that allow them to fly efficiently [34]. One of them is that their wings are composed of several feathers instead of a continuous

surface [30]. Each flight feather is made of a central structure and one vane at each side that overlaps with the vane from the opposite side of the adjacent feather [8]. This overlap enables the feathers to partially slide along each other, allowing the bird to adapt the wing geometry during flight, which allows them to fly in tight spaces, such as between tree branches in dense vegetation, or to fly faster to increase their hunting efficacy. This feature is explored to design Unmanned Aerial Vehicles (UAV) maneuvering similar to birds [26], to reduce the drag and increase the maximum speed [7, 1, 5, 18].

Each flight feather is an extremely lightweight and flexible structure that interacts with the airflow in a complex interplay of aerodynamics, structural dynamics, and vehicle dynamics. Being individually clamped to the wing, each feather can deform relatively independently of the others [32]. The feathers are clamped with their vanes overlapping, with the distal vane of a proximal feather placed over the proximal vane of a distal feather. This overlapping configuration defines a region of contact and results in an interesting dynamic mechanism observed during flapping flight characterized by the separation and contact between feathers during the flapping motion, as shown in Fig. 1. The separation of the feathers creates a clearance for the air to flow through, which increases the aerodynamic efficiency of the flapping cycle by reducing the negative contribution to the lift during the upstroke [38]. On the other hand, when the forces are acting from below, the deformation of the feathers is coupled due to the contact between the overlapping vanes.

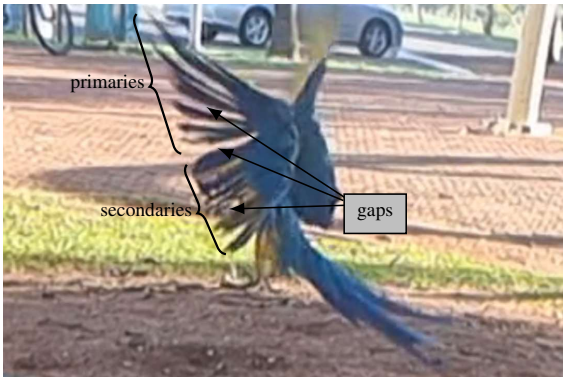


Figure 1: Observation of bird flight shows gaps between the flight feathers during its flapping motion.

Contact is classified as a boundary nonlinearity, and physically it consists that bodies can not penetrate each other during their motion [21], which is the impenetrability condition [16]. The contact between components is present in several problems, such as the contact between beams [33], plates [23], and elements in a multibody system [15, 27]. The contact problem is expressed as nonlinear inequalities by Karush-Kuhn-Tucker condition: $g \geq 0,\ \lambda \leq 0, g\lambda = 0$: where the contact-force in this expression $\lambda \leq 0$ are compressive, the gap $g \geq 0$ is equal or greater than zero, and the contact-force is zero

while the bodies are separated or the gap is zero and vice-versa [36]. However, solving the problem in this form of inequalities is challenging, and a typical approach consists of allowing but penalizing the penetration between the bodies at the expense of computing a set of opposing forces on the contacting surfaces in a continuous-contact formulation [10].

Although exists UAV with feathered wing designs, the focus is on the morphing feature for the advantages discussed previously, where the separation and contact of the airfoils during a flapping motion is not discussed. The context of this work is a step towards the development of flapping wing unmanned aerial vehicles (FWUAV), and instead of focusing on traditional wing designs, which often inherit design concepts from classical aircraft, we investigate the advantages of incorporating bioinspired features into the design of flapping wing vehicles. To this end, this work presents a modeling approach for a feathered wing design with multiple airfoil surfaces undergoing a flapping motion. In this configuration, the airfoils are flexible, which deform during the flapping cycle, and we discuss the contribution of the structural dynamics and clamping position of each airfoil to the deformation of the airfoils during a typical flapping motion.

The remaining part of the text is organized as follows: Section 2 presents the kinematic description of the contacting feathers and how the equation of motion is obtained. Section 3 presents the line-to-line contact formulation and the continuous-contact force model for the overlapping airfoils. Section 4 presents an analysis of the time-response from the multi-airfoil wing models during a sinusoidal flapping motion. Section 5, we present the final remarks of this work.

2 FORMULATION OF THE BIOINSPIRED MULTI-AIRFOIL FLAPPING WING MODEL

This section introduces the bioinspired model and the derivation of the DAE system that represents its dynamics.

Figure 2 shows the feathered wing and kinematic parameters defining the system under consideration, with a bird illustrated to indicate how the model parts correspond to the flapping wing. The model is simplified by considering a rigid wing attached to a spherical joint at B and two coordinate system namely: the inertial $\mathscr{I} : \{O, x, y, z\}$ and the body $\mathscr{B} : \{O, {}_{\mathscr{B}}x, {}_{\mathscr{B}}y, {}_{\mathscr{B}}z\}$ coordinate systems. This joint constraint one end of the rigid wing while enabling rotations along all three axes, therefore, this rigid wing part has three rotational degrees of freedom, which consists of [11]: up and down flapping rotation (with respect to x-axis), a spanning rotation with respect to the vertical-axis, and a pitch rotation consisting of a rotation with respect to the wing-axis. These motions are combined in a flapping pattern that depends on the requirements for lift and thrust of each flight phase.

Several airfoils are positioned along this rigid wing with their sides overlapping. In a given pair of airfoils (represented in the figure by $F^{(1)}$ and $F^{(2)}$), the one closer to the body is denoted as the proximal structure, whereas the other one is the distal feather. Each airfoil consists of a thin rectangular surface, and its structure is represented as an ANCF beam element.

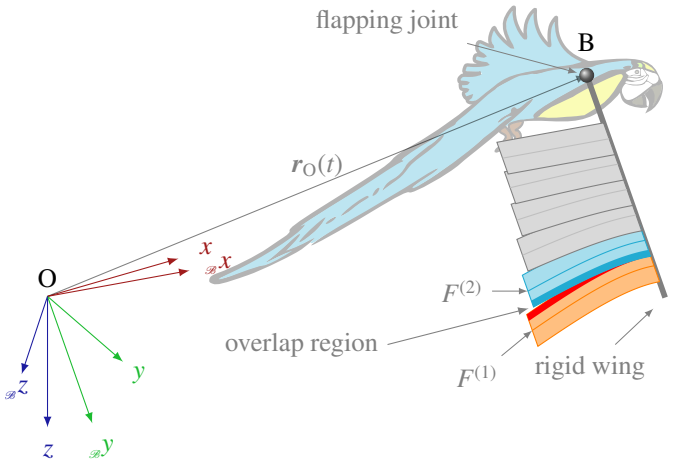


Figure 2: Illustration of the multi-airfoil wing model system and its kinematic parameters.

2.1 Airfoil model based on Absolute Nodal Coordinate Formulation

The dynamics of the airfoil structure is formulated using the Absolute Nodal Coordinate Formulation (ANCF). The position vector of a particle of an ANCF element is defined by an interpolation polynomial that is cubic in the longitudinal direction, and linear in the transverse directions for a three-dimensional beam element [37]. The nodal coordinate vector of the mth beam element, referenced by the subscript $(\cdot)_m$, is defined by the position and slopes in an absolute frame as:

$$\boldsymbol{e}_m = \left[\boldsymbol{r}^{i\top} \quad \boldsymbol{r}_x^{i\top} \quad \boldsymbol{r}_y^{i\top} \quad \boldsymbol{r}_z^{i\top} \quad \boldsymbol{r}^{j\top} \quad \boldsymbol{r}_x^{j\top} \quad \boldsymbol{r}_y^{j\top} \quad \boldsymbol{r}_z^{j\top}\right]^\top \tag{1}$$

with i and j denoting the first (left-hand side) and last (right-hand side) nodes of the beam-element, and $\boldsymbol{r}_\alpha^k = \frac{\partial \boldsymbol{r}^k}{\partial \alpha}, \alpha = x, y, z$, denotes the slope vector in the α direction of the kth node. The slope with respect to the x direction is tangent to the beam centerline, whereas on the y and z directions, non-orthogonal in general, define the plane of the cross-section. The position along this element is obtained in terms of its nodal coordinates through a shape function defined as:

$$\boldsymbol{r} = \boldsymbol{S}\boldsymbol{e}_m, \tag{2}$$

where $\boldsymbol{S}$ is the element shape function, and

$$\boldsymbol{S} = \boldsymbol{s} \otimes \boldsymbol{I}, \tag{3}$$

where $\boldsymbol{s} = \{s_1 \; s_2 \; \dots \; s_8\}$, $\boldsymbol{I}$ is a 3×3 identity matrix and $\otimes$ is the Kronecker product. The coefficients of Eq. 3 are defined as:

$$\begin{aligned} s_1 &= 1 - 3\xi^2 + 2\xi^3, \quad & s_2 &= l\left(\xi - 2\xi^2 + \xi^3\right), \quad & s_3 &= l(\eta - \xi\eta), \quad & s_4 &= l(\zeta - \xi\zeta) \\ s_5 &= 3\xi^2 - 2\xi^3, & s_6 &= l(-\xi^2 + \xi^3), & s_7 &= l\xi\eta, & s_8 &= l\xi\zeta. \end{aligned} \tag{4}$$

where the non-dimensional coordinates $\xi = \frac{x}{l}$, $\eta = \frac{y}{l}$ and $\zeta = \frac{z}{l}$ are defined, and l is the element length. Figure 3 illustrates the ANCF beam element in a generic deformed configuration and a representation of the nodal coordinates.

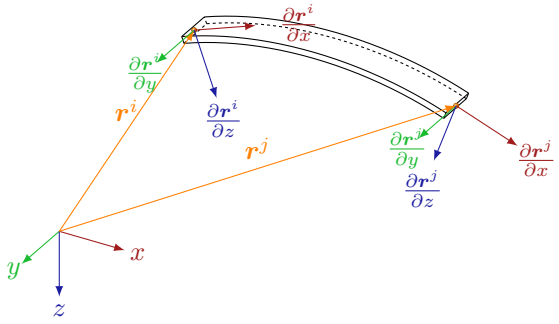


Figure 3: Depiction of the ANCF beam element and its nodal coordinates used to represent each airfoil structure in a general deformed configuration.

2.2 Assembly of the system matrices and vectors

The ith airfoil structure, indicated by the superscript $(\cdot)^{(i)}$, is discretized into n_{mesh} ANCF beam elements, with $n_{\text{nodes}} \equiv (n_{\text{mesh}} + 1)$ nodes. The nodal coordinate vector of the ith structure is obtained by constructing a vector of dimension $12 \times n_{\text{nodes}}$, where the entries are the position and slope vectors of each consecutive node:

$$\boldsymbol{e}^{(i)} = \left[\boldsymbol{r}^{1\top} \quad \boldsymbol{r}_x^{1\top} \quad \boldsymbol{r}_y^{1\top} \quad \boldsymbol{r}_z^{1\top} \quad \cdots \quad \boldsymbol{r}^{n_{\text{nodes}}\top} \quad \boldsymbol{r}_x^{n_{\text{nodes}}\top} \quad \boldsymbol{r}_y^{n_{\text{nodes}}\top} \quad \boldsymbol{r}_z^{n_{\text{nodes}}\top}\right]^\top \tag{5}$$

The nodal coordinate vector of the system is composed by joining the nodal coordinate vector of each structure, and it is represented by considering the coordinates from n_F airfoils as follows:

$$\boldsymbol{e} = \left[\boldsymbol{e}^{(1)\top} \quad \boldsymbol{e}^{(2)\top} \quad \cdots \quad \boldsymbol{e}^{(n_F)\top}\right]^\top \tag{6}$$

The global matrices of the system are defined similarly by allocating the terms associated with each structure to a block diagonal global matrix:

$$\boldsymbol{M} = \begin{bmatrix} \boldsymbol{M}^{(1)} & & & \\ & \boldsymbol{M}^{(2)} & & \\ & & \ddots & \\ & & & \boldsymbol{M}^{(n_F)} \end{bmatrix}, \tag{7}$$

where $\boldsymbol{M}^{(i)}$ is the mass matrix of the ith structure obtained after assembling the mass matrix of its composing ANCF elements.

2.3 Flapping constraints

This section describes how the flapping motion is imposed in terms of the nodal coordinates of the ANCF beam element.

The flapping motion under consideration consists of a rotation of the rigid wing with respect to the $x-$axis by a time-parameterized flapping angle $\alpha_F(t)$. The rotation matrix to map a vector from the body to the inertial system is defined by:

$$\boldsymbol{R}(t) = \begin{bmatrix} 1 & 0 & 0 \\ 0 & \cos(\alpha_F(t)) & -\sin(\alpha_F(t)) \\ 0 & \sin(\alpha_F(t)) & \cos(\alpha_F(t)) \end{bmatrix}. \tag{8}$$

Each ith airfoil structure is clamped along the rigid wing at a distance $l_p^{(i)}$ of the joint B along the rigid wing structure on the ${}_{\mathscr{B}}y$-axis. Therefore, the position vector of the clamping is defined in the body reference frame as:

$${}_{\mathscr{B}}\boldsymbol{l}_p^{(i)} = \begin{Bmatrix} 0 & l_p^{(i)} & 0 \end{Bmatrix}^\top. \tag{9}$$

The first node of each airfoil has its position and slopes constrained according to the following constraint equations:

$$\boldsymbol{\Phi}^{(i)}(t, \boldsymbol{e}^{(i)}) = \begin{Bmatrix} \boldsymbol{r}^1 - \boldsymbol{R}\,{}_{\mathscr{B}}\boldsymbol{l}_p^{(i)} \\ \boldsymbol{r}_x^1 - \boldsymbol{R}(:,1) \\ \boldsymbol{r}_y^1 - \boldsymbol{R}(:,2) \\ \boldsymbol{r}_z^1 - \boldsymbol{R}(:,3) \end{Bmatrix} = \boldsymbol{0}, \tag{10}$$

where $\boldsymbol{R}(:,i)$ indicate the vector formed by ith column of the transformation matrix. The constraint vector of the system is assembled by considering

$$\boldsymbol{\Phi}(t, \boldsymbol{e}) = \begin{Bmatrix} \boldsymbol{\Phi}^{(1)\top} & \boldsymbol{\Phi}^{(2)\top} & \cdots & \boldsymbol{\Phi}^{(n_F)\top} \end{Bmatrix}^\top \tag{11}$$

2.4 DAE integration

The resulting model is an index-3 *Differential Algebraic Equation* (DAE) system as follows:

$$\boldsymbol{M}\ddot{\boldsymbol{e}} + \boldsymbol{\Phi}_e^\top \boldsymbol{\Lambda} - \boldsymbol{f} = \boldsymbol{0} \tag{12}$$

$$\boldsymbol{\Phi}\,(t, \boldsymbol{e}) = \boldsymbol{0}. \tag{13}$$

The dependency of the system on the flapping constraints is introduced by the constraint forces in the second term of the differential equation through the Lagrange multiplier vector $\boldsymbol{\Lambda}$ projected to the space associated with the nodal coordinates by the Jacobian of the constraint equations $\boldsymbol{\Phi}_e$. The vector $\boldsymbol{f} = \boldsymbol{f}^{\text{ela}} + \boldsymbol{f}^{\text{damp}} + \boldsymbol{f}^{\text{con}}$ comprises the forces

originated from different sources: (a) due to the elastic potential, (b) due to a viscoelastic internal damping model, and (c) due to the contact-forces. The formulation for the contact forces is described in the following sections.

The DAE system is solved in an iterative fashion using the generalized-α algorithm [2].

$$(1-\alpha_m)\,\boldsymbol{a}[k+1] + \alpha_m \boldsymbol{a}[k] = \left(1-\alpha_f\right)\ddot{\boldsymbol{e}}[k+1] + \alpha_f \ddot{\boldsymbol{e}}[k], \qquad \boldsymbol{a}[0] = \ddot{\boldsymbol{e}}[0]. \tag{14}$$

Vector $\boldsymbol{a}$ in Eq. (14) is an auxiliary variable and the index $k \in \mathbb{Z}$ inside the bracket indicates a designated instant from the discretized time $t = k\Delta t$, with Δt being the time-step. In addition $\alpha_m = \frac{2\rho_\infty - 1}{\rho_\infty + 1}$, $\alpha_f = \frac{\rho_\infty}{\rho_\infty + 1}$, and $0 \leq \rho_\infty \leq 1$ is the numerical dissipation factor (spectral ratio) used in the simulation, with a value of 1 representing no dissipation and 0 representing asymptotic annihilation [6]. The generalized-α scheme is obtained using the following Newmark formulas [2]:

$$\boldsymbol{e}[k+1] = \boldsymbol{e}[k] + \Delta t \dot{\boldsymbol{e}}[k] + \Delta t^2 \left(\frac{1}{2} - \beta\right)\boldsymbol{a}[k] + \Delta t^2 \beta \boldsymbol{a}[k+1], \tag{15}$$

$$\dot{\boldsymbol{e}}[k+1] = \dot{\boldsymbol{e}}[k] + \Delta t\,(1-\gamma)\,\boldsymbol{a}[k] + \Delta t \gamma \boldsymbol{a}[k+1]. \tag{16}$$

The predictions are used to evaluate Eqs. 12 and 13. If the residuals from this evaluation of the differential part, $\boldsymbol{r_e}$, and the constraint, $\boldsymbol{r_\Lambda}$, equations are within a tolerance, then this solution for the $k+1$ step is accepted. Otherwise, the dynamic of the system is linearized, and the solution of this linear version is used to update the predictions. To this end, the iteration matrix $\boldsymbol{S}_T$ is defined as:

$$\boldsymbol{S}_T = \begin{bmatrix} \boldsymbol{K}_T + \gamma' \boldsymbol{C}_T + \beta' \boldsymbol{M} & \boldsymbol{\Phi}_{\boldsymbol{e}}^\top \\ \boldsymbol{\Phi}_{\boldsymbol{e}} & \boldsymbol{0} \end{bmatrix} \tag{17}$$

where $\boldsymbol{K}_T$ is the tangent stiffness matrix:

$$\boldsymbol{K}_T = -\left(\frac{\partial \boldsymbol{f}^{\text{ela}}}{\partial \boldsymbol{e}} + \frac{\partial \boldsymbol{f}^{\text{damp}}}{\partial \boldsymbol{e}} + \frac{\partial \boldsymbol{f}^{\text{con}}}{\partial \boldsymbol{e}}\right), \tag{18}$$

and $\boldsymbol{C}_T$ is the tangent damping matrix:

$$\boldsymbol{C}_T = -\left(\frac{\partial \boldsymbol{f}^{\text{damp}}}{\partial \dot{\boldsymbol{e}}} + \frac{\partial \boldsymbol{f}^{\text{con}}}{\partial \dot{\boldsymbol{e}}}\right). \tag{19}$$

The computation of the tangent stiffness and damping matrices is required at each iteration step. Since these forces are derived from a quadrature within each element domain, they are computationally expensive to evaluate. Furthermore, obtaining the Jacobian using finite differences amplifies this issue. An efficient solution is to compute these terms using invariant matrices presented in [12, 13], which enable factorizing the nodal coordinates from the quadrature and computing them once in advance.

At each iteration step, the following linear system of equations is solved for the correction values of the nodal coordinate vector and Lagrange multipliers:

$$\begin{Bmatrix} \Delta \boldsymbol{e} \\ \Delta \boldsymbol{\Lambda} \end{Bmatrix} = -\boldsymbol{S}_T^{-1} \begin{Bmatrix} \boldsymbol{r_e} \\ \boldsymbol{r_\Lambda} \end{Bmatrix}. \tag{20}$$

The solution for the current step is accepted if the residual is less than a predetermined tolerance, which for this work is chosen as 10^{-6}. The parameters for the generalized-α method are

$$\beta' = \frac{1 - \alpha_m}{\Delta t^2 \beta (1 - \alpha_f)} \tag{21}$$

$$\gamma' = \frac{\gamma}{\Delta t \beta} \tag{22}$$

and [6]

$$\beta = (1 - \alpha_m + \alpha_f)^2/4 \tag{23}$$

$$\gamma = 1/2 - \alpha_m + \alpha_f \tag{24}$$

3 FORMULATION OF THE CONTACT MODEL

This section presents the contact model for the overlapping airfoils. The contact search is addressed where the contact kinematic parameters are defined, and the region of potential contact is monitored to check whether the bodies are in contact or separated. Then, the nodal contact force is obtained considering the ANCF discretization.

Contact analysis is divided into three procedures: contact-search, contact-detection, and the contact-force model. (a) In the contact search, the surfaces that may come into contact are defined in advance, and their points are monitored to check whether they are penetrating other portions of the body. (b) Contact detection consists of computing precisely the instant of the contact. This step is important for continuous-contact models since the inaccurate detection may lead to excessive penetration between the bodies when the contact is first detected, resulting in unrealistic contact forces and convergence issues [9]. (c) The contact-force procedure consists of modeling the force between bodies in the contact regions. For this work, a contact force proportional to the penetration is used to limit the penetration between the bodies.

Several approaches exist to model the contact: a point-to-point contact model where one solves for the closest point of two bodies in a bilateral minimal distance problem, and includes the contact forces solely at this point. This setting is adequate for problems where the contact is confined to a small region, for example, between stiff bodies with non-conforming geometries [19]. On the other hand, for problems such as the contact

between the airfoils herein, the bodies have a conforming geometry, since one airfoil deforms into a convex shape, whereas the other into a concave shape that fits during the contact. In this case, the contact regions rapidly increase with the deformation, and the assumption of a single point is not representative of the problem. Instead, the line-to-line contact formulation considers that the contact forces are distributed, and it is more adequate for the problem [29]. In the line-to-line contact, the contact forces are treated as a distribution over the contact line.

3.1 Contact Search

Contact search consists of defining and measuring the distance between points on the boundaries that may contact with each other during their motion. The terminology herein is the following: one boundary is denoted as the contactor and the other as the target, with the distal and proximal airfoils assuming these roles, respectively [21]. The superscript $(\cdot)^{(i)}$ indicates that the corresponding term is associated with the ith structure. Moreover, without loss of generality, the contactor and target are indicated by the numbers 1 and 2, respectively.

The contact is assumed to occur along a contact line at the middle of the overlapping region. In addition, since the airfoil's structure is thin, the contact is evaluated at the middle section of each beam, i.e., $\zeta = 0$. The contact is evaluated at points on the contact line corresponding to the collocation points of a Gauss quadrature [22].

Given a point of the contactor along the contact-line parameterized as $x^{(1)} \in [0, l_f^{(1)}]$ with corresponding position vector $\boldsymbol{r}^{(1)} \equiv \boldsymbol{r}^{(1)}(x^{(1)})$, the closest point from the target surface, $\boldsymbol{r}^{(2)} \equiv \boldsymbol{r}^{(2)}\left(x^{(2)}\left(x^{(1)}\right)\right)$, is geometrically the position where a fictitious line connecting these positions is orthogonal to the target surface.

$$\left(\boldsymbol{r}^{(1)} - \boldsymbol{r}^{(2)}\right)^{\top} \boldsymbol{t}^{(2)} = 0 \tag{25}$$

where $\boldsymbol{t}^{(2)} \equiv \boldsymbol{t}^{(2)}\left(x^{(2)}\left(x^{(1)}\right)\right)$ is the vector tangent to the surface of the target at $x^{(2)}\left(x^{(1)}\right)$.

Each contact pair $\left\{x^{(1)},\ x^{(2)}\left(x^{(1)}\right)\right\}$ is obtained by solving Eq. (25) using the bisection algorithm according to the following procedure: for a given point on the contactor structure, a scan procedure of the target beam elements begin where the first and last nodes of the ith ANCF element, i.e. $\xi = 0$ and $\xi = 1$, are scanned to check the sign of the residual from Eq. (25). If the signs are equal, then the closest point is not on this element, and the next is verified. If the sign differs, then the solution for the closest point projection is within this element. Then, the interval is partitioned in half, and the sign of the residual at the middle of the interval is compared and substituted into a smaller interval. This partitioning process repeats until the residual is smaller than a determined tolerance, and the solution for

the closest point projection is obtained.

The gap between a contact pair is measured by

$$g\left(x^{(1)}\right) = \left(\boldsymbol{r}^{(1)} - \boldsymbol{r}^{(2)}\right)^{\top} \boldsymbol{n}^{(2)}, \tag{26}$$

with $\boldsymbol{n}^{(2)} \equiv \boldsymbol{n}^{(2)}\left(x^{(2)}\left(x^{(1)}\right)\right)$ denoting the normal unit vector at $\boldsymbol{x}^{(2)}$. The kinematic parameters of the contact search are illustrated in Fig. 4. In this figure, the contact line of the two airfoils is represented in the ${}_{\mathscr{B}}(xz)$ plane, which is a suitable plane to visualize vertical deformation of the airfoil's structure. The contactor and target structures are separated if the gap is positive, and the equations of motion are obtained as usual. If the gap is negative, this means that one body is penetrating the other.

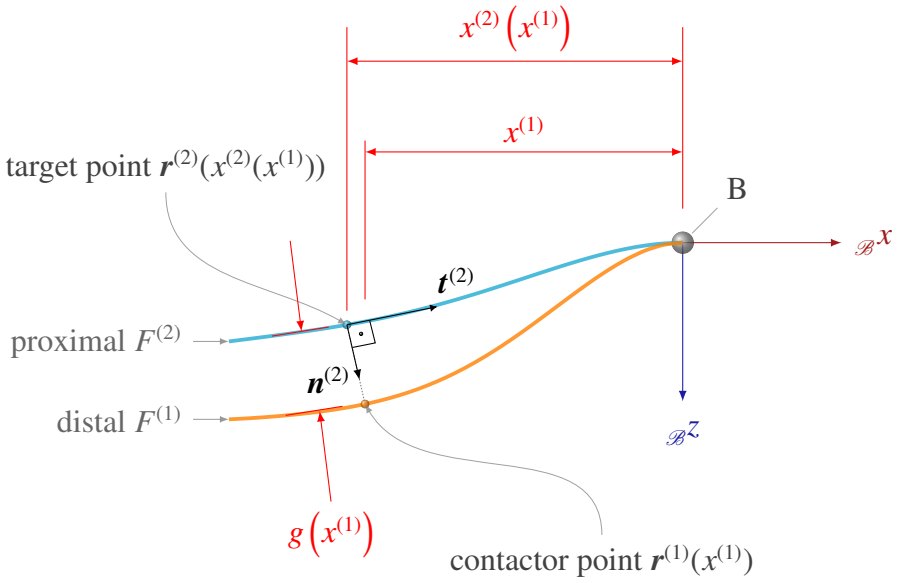


Figure 4: Representation of the contact line of each structure in the ${}_{\mathscr{B}}(xz)$ plane illustrating the variables of the contact search.

3.2 Contact force model

In the continuous-contact formulation, no restriction is made to the coordinates and the bodies are allowed to penetrate each other. However, the tendency for the penetration of bodies is opposed by including a force on the contacting regions, defined according to the following equation:

$$f_c = \begin{cases} 0, & \text{if } \epsilon < 0 \\ k_c \epsilon, & \text{otherwise.} \end{cases} \tag{27}$$

It consists of an elastic force component proportional to the penetration between the bodies, which is defined as the negative of the gap:

$$\epsilon \equiv -g, \tag{28}$$

such that a positive value is evaluated when the bodies are contacting, *i.e.*, $\epsilon \geq 0$.

3.3 Nodal contact-forces and Jacobian

The virtual work due to contact-forces is defined according to the following equation:

$$\delta W^{\text{con}} = \int_{\Omega} f_c \delta g d\Omega, \tag{29}$$

where the integral is performed along the contact line boundary Ω. The variation of the gap is obtained according to [4, 31]:

$$\delta g = \left(\delta \boldsymbol{r}^{(1)} - \delta \boldsymbol{r}^{(2)}\right)^{\top} \boldsymbol{n}^{(2)}. \tag{30}$$

The contact line is split into several boundaries $\Omega = [\Omega_1,\ \Omega_2,\ \cdots,\ \Omega_{n_{\text{mesh}}}]$, where each Ω_i boundary spans the ith ANCF element of the contactor structure. Therefore, the integrals are evaluated by:

$$\int_{\Omega} (\cdot) d\Omega = \int_{\Omega_1} (\cdot) d\Omega + \int_{\Omega_2} (\cdot) d\Omega + \cdots + \int_{\Omega_{n_{\text{mesh}}}} (\cdot) d\Omega. \tag{31}$$

Therefore, the variations of the position can be expressed in terms of variations of the nodal coordinates as:

$$\delta \boldsymbol{r} = \boldsymbol{S} \delta \boldsymbol{e}. \tag{32}$$

Splitting the contact boundary from Eq. (29) and substituting the variation from the position for the nodal coordinates according to Eq. (32), the following expression is obtained for the virtual work of the mth element:

$$\delta W_m^{\text{con}} = \int_{\Omega_m} f_c \left(\boldsymbol{S}(x^{(1)}) \delta \boldsymbol{e}_m^{(1)} - \boldsymbol{S}(x^{(2)}) \delta \boldsymbol{e}_t^{(2)}\right)^{\top} \boldsymbol{n}^{(2)} d\Omega, \tag{33}$$

which can be expressed as:

$$\delta W_m^{\text{con}} = \delta \boldsymbol{e}_m^{(1)\top} \boldsymbol{Q}_m^{(1)} + \delta \boldsymbol{e}_t^{(2)\top} \boldsymbol{Q}_t^{(2)}, \tag{34}$$

where the nodal contact-force vector for the contact-pair are identified as:

$$\boldsymbol{Q}_m^{(1)} = \int_{\Omega_m} f_c \boldsymbol{S}(x^{(1)})^{\top} \boldsymbol{n}^{(2)} d\Omega, \tag{35}$$

$$\boldsymbol{Q}_t^{(2)} = -\int_{\Omega_m} f_c \boldsymbol{S}(x^{(2)})^{\top} \boldsymbol{n}^{(2)} d\Omega. \tag{36}$$

These forces are inserted in the numerical procedure by evaluating the integrals from Eqs. (35-36) at collocation points according to a Gauss quadrature. The Jacobian of the nodal contact-force is necessary for the generalized-α method as shown in Eqs. (18-19). The Jacobian of these contact forces with respect to the nodal coordinates of the system is evaluated approximately as follows

$$\frac{\partial \boldsymbol{Q}_c^{(1)}}{\partial \boldsymbol{e}_m^{(1)}} = \int_{\Omega_m} n\epsilon^{n-1}\left(k_c + \chi\dot{\epsilon}\right) \boldsymbol{S}(x^{(1)})^\top \boldsymbol{n}^{(2)} \boldsymbol{n}^{(2)^\top} \boldsymbol{S}(x^{(1)}) d\Omega \tag{37}$$

$$\frac{\partial \boldsymbol{Q}_c^{(1)}}{\partial \boldsymbol{e}_t^{(2)}} = -\int_{\Omega_m} n\epsilon^{n-1}\left(k_c + \chi\dot{\epsilon}\right) \boldsymbol{S}(x^{(1)})^\top \boldsymbol{n}^{(2)} \boldsymbol{n}^{(2)^\top} \boldsymbol{S}(x^{(2)}) d\Omega \tag{38}$$

and

$$\frac{\partial \boldsymbol{Q}_c^{(2)}}{\partial \boldsymbol{e}_m^{(1)}} = -\int_{\Omega_m} n\epsilon^{n-1}\left(k_c + \chi\dot{\epsilon}\right) \boldsymbol{S}(x^{(2)})^\top \boldsymbol{n}^{(2)} \boldsymbol{n}^{(2)^\top} \boldsymbol{S}(x^{(1)}) d\Omega \tag{39}$$

$$\frac{\partial \boldsymbol{Q}_c^{(2)}}{\partial \boldsymbol{e}_t^{(2)}} = \int_{\Omega_m} n\epsilon^{n-1}\left(k_c + \chi\dot{\epsilon}\right) \boldsymbol{S}(x^{(2)})^\top \boldsymbol{n}^{(2)} \boldsymbol{n}^{(2)^\top} \boldsymbol{S}(x^{(2)}) d\Omega \tag{40}$$

The Jacobian with respect to the nodal velocities is:

$$\frac{\partial \boldsymbol{Q}_c^{(1)}}{\partial \dot{\boldsymbol{e}}^{(1)}} = \int_{\Omega_m} \chi\epsilon^{n} \boldsymbol{S}(x^{(1)})^\top \boldsymbol{n}^{(2)} \boldsymbol{n}^{(2)^\top} \boldsymbol{S}(x^{(1)}) d\Omega \tag{41}$$

$$\frac{\partial \boldsymbol{Q}_c^{(1)}}{\partial \dot{\boldsymbol{e}}^{(2)}} = -\int_{\Omega_m} \chi\epsilon^{n} \boldsymbol{S}(x^{(1)})^\top \boldsymbol{n}^{(2)} \boldsymbol{n}^{(2)^\top} \boldsymbol{S}(x^{(2)}) d\Omega \tag{42}$$

$$\frac{\partial \boldsymbol{Q}_c^{(2)}}{\partial \dot{\boldsymbol{e}}^{(1)}} = -\int_{\Omega_m} \chi\epsilon^{n} \boldsymbol{S}(x^{(2)})^\top \boldsymbol{n}^{(2)} \boldsymbol{n}^{(2)^\top} \boldsymbol{S}(x^{(1)}) d\Omega \tag{43}$$

$$\frac{\partial \boldsymbol{Q}_c^{(2)}}{\partial \dot{\boldsymbol{e}}^{(2)}} = \int_{\Omega_m} \chi\epsilon^{n} \boldsymbol{S}(x^{(2)})^\top \boldsymbol{n}^{(2)} \boldsymbol{n}^{(2)^\top} \boldsymbol{S}(x^{(2)}) d\Omega \tag{44}$$

4 RESULTS AND DISCUSSION

This section presents results obtained by integration of the equation of motion of the multi-airfoil system undergoing a tapered sinusoidal flapping motion. A model with two representative airfoils is defined first, where the effect of different contact parameters is discussed. Then, the results for a wing with more airfoils are presented.

Convergence analysis

Considering the system parameters from Tab. 1, and assuming an equivalent structure clamped at the first node, the convergence of the natural frequencies for various mesh refinements is presented in Fig.5. The first mode converges faster than the remaining modes,

with a relative error of $e_{\%} = 0.20\%$ using 10 elements when comparing with the analytical value for the frequency of the first mode of an equivalent Euler-Bernoulli beam [24]. Increasing the number of elements further reduces this difference at the expense of increasing the computational cost.

Table 1: Structural, geometric and flapping parameters of the feathered flapping wing model.

parameter	**description**	**value**	**unit**
ρ	specific volume	2870	kg.m^{-3}
E	Young modulus	68.9×10^9	Pa
ν	Poisson coefficient	0	
γ_s	viscoelastic dissipation parameter	5×10^{-4}	-
γ_d	viscoelastic dissipation parameter	5×10^{-4}	-
$l_f^{(i)}$	structure length	200	mm
$w^{(i)}$	structure width	30	mm
$h^{(i)}$	structure height	0.5	mm

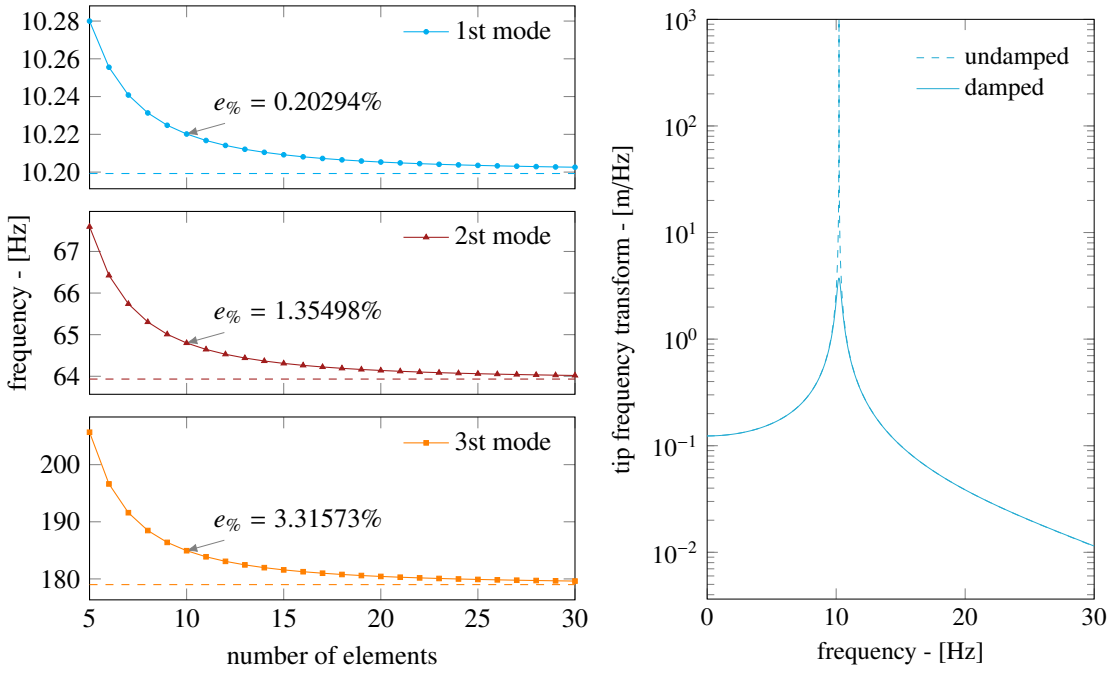


Figure 5: Structural properties of the airfoil structure: (a) convergence of the first three modes of the structure. The dashed lines indicate the analytical values for the bending frequency of a clamped-free Euler-Bernoulli beam [24]; (b) shows the frequency response functions of the tip vertical displacement of the undamped and with the viscoelastic damping model.

The flapping motion under investigation consists of a rotation of the wing with respect to the x axis by a time-varying angle $\alpha_F(t)$. In practice, other motions are combined with this one, either passive, through an aeroelastic coupling [11], or actively, since the kinematics

of the flapping alone yield a symmetric lift output during each cycle, which is unable to sustain a body in air [11]. Nonetheless, the results of the multi-airfoil wing model are discussed based on this single flapping motion alone and the effect of other combinations of motions is left for future investigations.

The flapping pattern is defined as a tapered sinusoidal varying signal represented by $\alpha_F(t) = s(t)a_F \sin(2\pi f_F)$ where a_F is the amplitude, f_F is the frequency in Hz, and $s(t)$ is a taper function that gradually increases the amplitude of the input to reduce impulsive transient vibrations and also allows the initialization of the nodal velocities vector of the system as zero. The taper function is defined as:

$$s(t;[a,b]) = \begin{cases} 0, & \text{if } t < a, \\ c_0 + c_1 t + c_2 t^2 + c_3 t^3 + c_4 t^4 + c_5 t^5 & \text{if } a \le t < b, \\ 1, & \text{if } b \le t \end{cases}$$

where the coefficients of the polynomial $c_i, i = 0, \ldots, 5$ are obtained by solving an algebraic system of equations consisting of the values of the function and its first and second time derivatives evaluated at $t = a$ and $t = b$. Considering the start from zero, i.e. $a = 0$, the non-zero coefficients of Eq. (4) are $c_3 = 10b^{-3}$, $c_4 = -15b^{-4}$, $c_5 = 6b^{-5}$. All simulations are performed with a constant flapping amplitude and frequency of $a_F = 30°$ and $f_F = 1$ Hz, respectively. The time variation during one cycle of the angular velocity and acceleration functions of a sinusoidal flapping pattern after the transient is presented in Fig. 6. The flapping cycle can be divided into two periods: the upstroke, starting with the wings at the lowest position moving upwards, and the downstroke, starting with the wings at the most elevated position and moving downwards. The rigid wing is illustrated at the start of each phase and at intermediate positions.

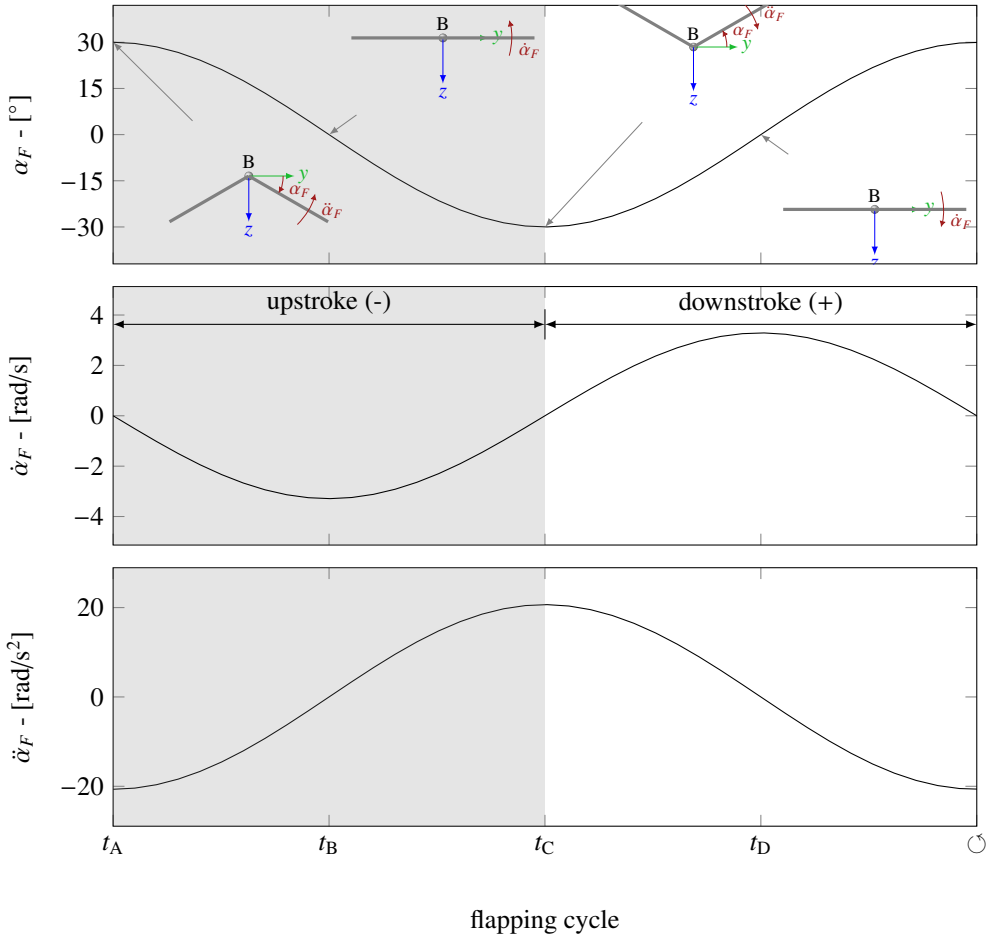


Figure 6: Representation from the kinematics of the flapping wing during the flapping cycle. The upstroke and downstroke periods are delimited and indicated by (-) and (+), respectively.

At the start of the upstroke, the wing is at the lowest position, as indicated in the figure at t_A. At this instant, the angular velocity is zero and the angular acceleration is at one of its peaks. After this instant, the angular velocity and acceleration signals are both negative until half of the upstroke. At the middle of the upstroke, t_B, the wing crosses the mid-plane and the angular velocity is at the peak, whereas the angular acceleration is zero. After this instant, they have opposite signals until the wing reaches the uppermost position, t_C to start the downstroke. After this moment, the angular velocity is zero, the angular acceleration is at its highest, and they have the same sign. The wing moves in the downwards direction until it crosses the middle plane, t_D, with zero angular acceleration and the highest velocity. After this moment, they have opposite signs until the start of the next flapping cycle. In this sequence of events, the angular acceleration is at its highest during the stroke reversal, that is, at t_A and t_C. At these moments, the inertial loads are high and mainly responsible for the airfoil deformation [17].

A model with two airfoils, $n_F = 2$, with the distal and proximal airfoils positioned at $l_p^{(1)} =$

0.30 m and $l_p^{(2)} = 0.28$ m, respectively, is defined to discuss the contact and separation between the airfoils during the flapping motion. Fig. 7 presents the gap measured at the tip of the contacting structure with respect to the closest point projection on the target. The result for $k_c = 0$ N/m presents the result of the contact search without considering the contact forces, that is, only the measurement of the gap is presented. Note that there are periods where penetration occurs, i.e., $g \leq 0$. The result of including the contact forces in the model is shown by the lines $k_c = [1, 10, 100]$ N/m in the figure. In this case, when indentation occurs, a set of contact forces is obtained opposing the bodies from penetrating the surface of the other. Therefore, the negative region of the graph is significantly reduced. It is also possible to note oscillations of the measured gap, which indicate that the airfoil vibrates in opposite directions after the contact release.

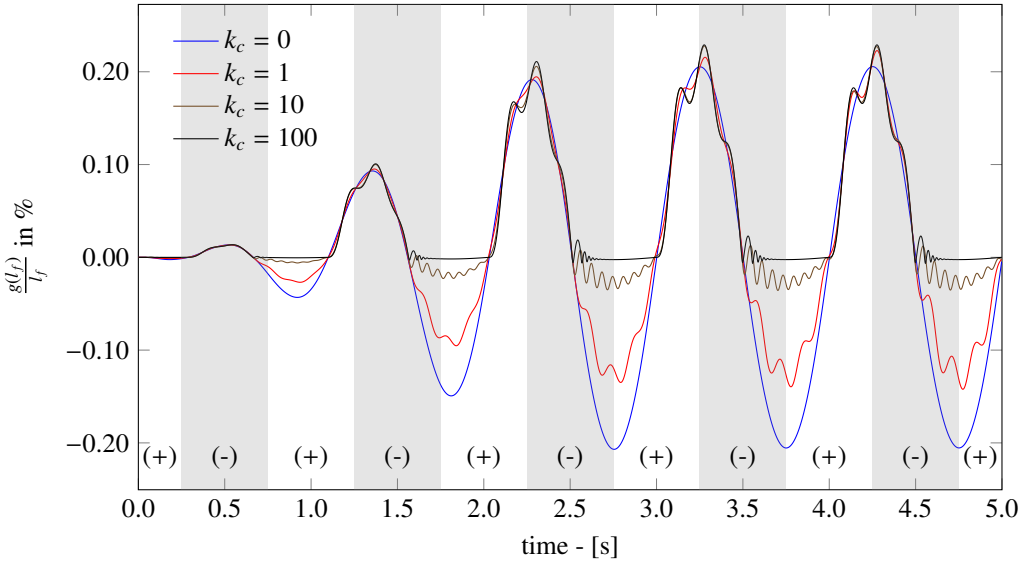


Figure 7: Gaps between the tips of adjacent structures. The gap is normalized by the airfoil length l_f. Results obtained with a mesh $n_{\text{mesh}} = 10$ and $\Delta t = 0.001$ s.

Figure 8 shows the measurements of the gaps along the length of the airfoil during a flapping cycle. The contact-line of each airfoil is illustrated at four instants of time, corresponding to the t_A, t_B, t_C, and t_D in Fig. 8b-8e. At the start of the upstroke, t_A in Fig. 8b, the distal airfoil deforms more than the proximal and a gap is defined between them along the entire length. At t_B, the middle of the upstroke, the airfoils contact, and there is no deflection between the airfoils, which corresponds to one of the instants of zero angular acceleration. At t_C, the start of the downstroke, the airfoils show an upward deflection; however, in this case, the distal cannot deflect more than the proximal due to the overlap and the result is airfoils in contact. At the middle of the downstroke, t_D, the airfoils show no deflection and no contact. After this instant is the beginning of the airfoil separation until the start of the upstroke of the next cycle.

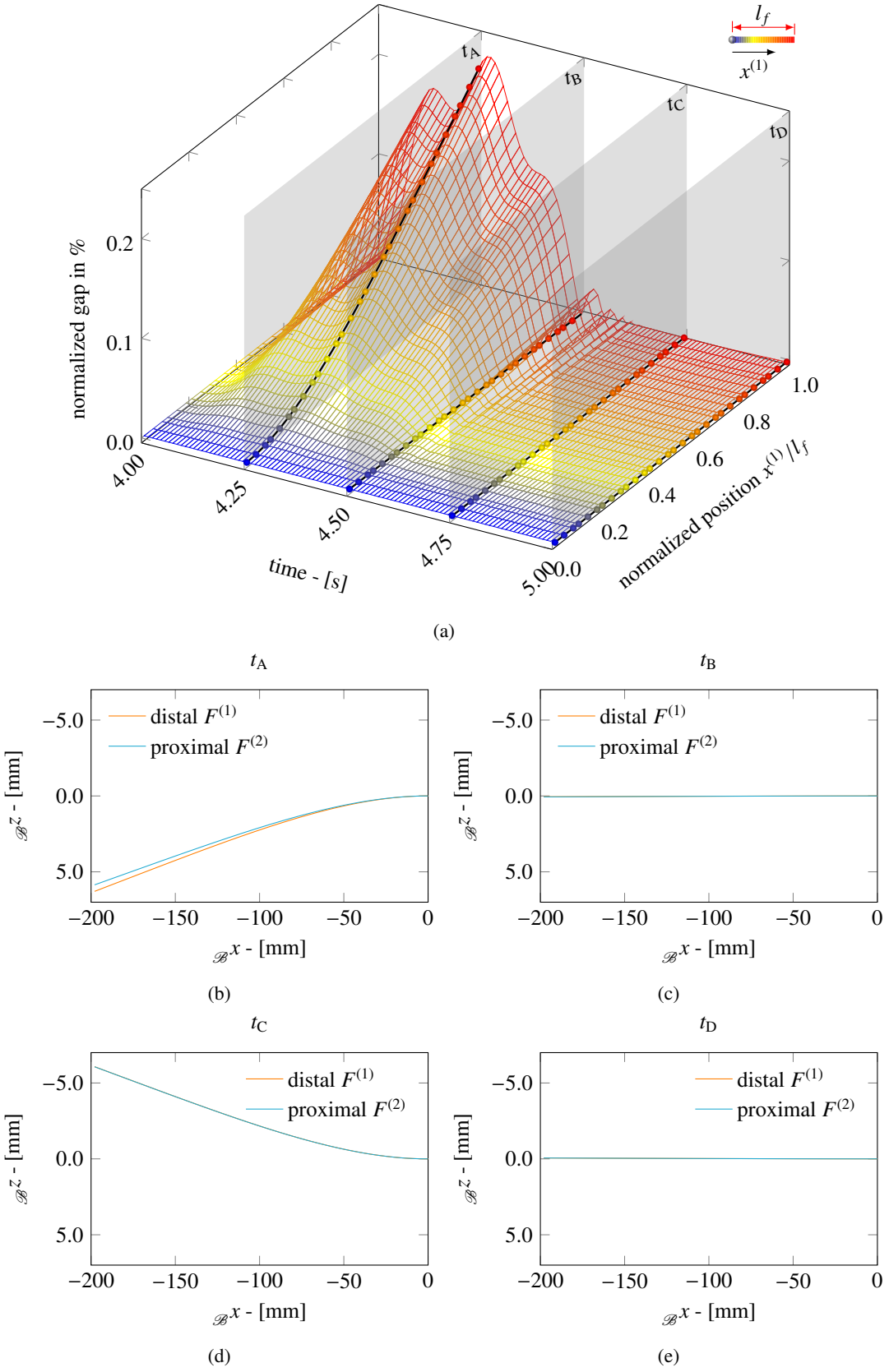
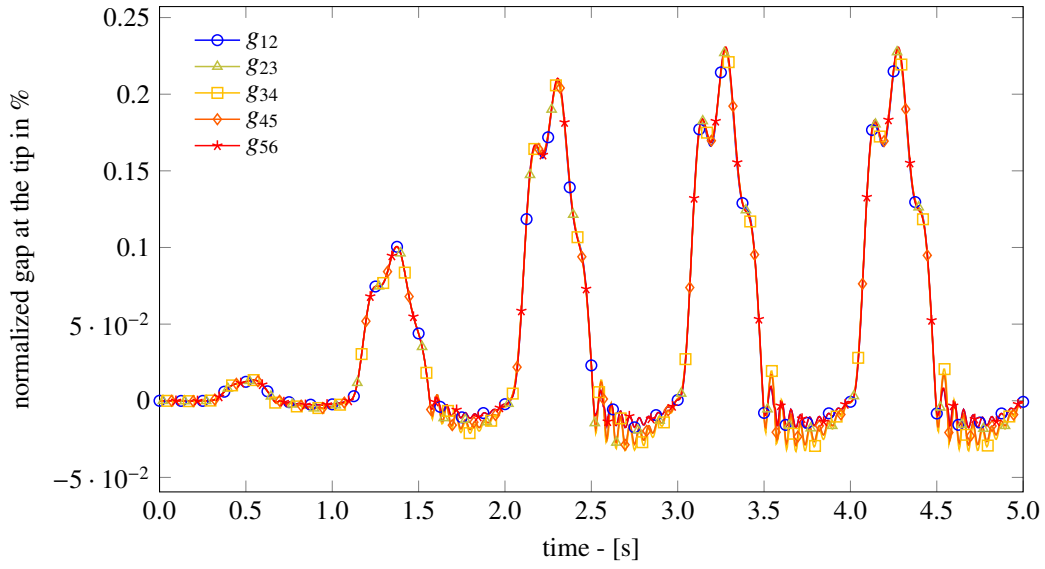


Figure 8: (a) Gap along the length during a flapping cycle considering $k_c = 100$ N/m and $c_r = 1$. Illustration of the airfoil configuration at different instants with respect to the flapping cycle: (b) start of the upstroke; (c) the middle of the upstroke; (d) start of the downstroke, and (e) middle of the downstroke.

Multi-airfoil wing model with uniform spacing

Now we consider a wing model with $n_F = 6$ airfoils with an uniform spacing of 20 mm, with the most distal airfoil positioned at $l_p^{(1)} = 300$ mm. In this configuration, there are 5 pairs and therefore 5 regions of potential contact where the contact forces are included ($k_c = 10$ N/m, $c_r = 1$, $n = 1$). The index-3 DAE system is solved using the generalized-α algorithm ($\rho_\infty = 0.25$, $\Delta t = 0.001$ s). The measurement of the gap between each pair of airfoils, shown in Fig. 9, indicates that this configuration with uniform airfoil distance yields gaps with approximately the same magnitude.



(a)

Figure 9: Simulation of the multi-airfoil wing with 6 airfoils undergoing a sinusoidal flapping motion with amplitude $a_F = 30°$ at a frequency of 1 Hz. (a) gaps. Illustration of the system configuration at: (b) downstroke. (c) upstroke

Multi-airfoil wing model with non-uniform spacing

A wing model with $n_F = 6$ airfoils and non-uniform spacing between them is considered. The clamping position from the most distal airfoil to the proximal, $l_p^{(i)}$, $i = 1, 2, \ldots, 6$ are defined as: [0.300 m, 0.275 m, 0.255 m, 0.240 m, 0.230 m, 0.225 m], which represents a distance of 5 mm between the closest pair ($F^{(5)}$ and $F^{(6)}$) and increasing with increments of 5 mm for each consecutive pair.

The result from this model with non-uniform spacing is presented in Fig. 10. The measurement of the gap between airfoils is presented in Fig. 10a, and it indicates that increasing the distance between airfoils increases the separation between the airfoils, and this relationship is linear. An additional consideration is that the spacing, considering airfoils of equal width, must be below their width, otherwise the contact can not occur since there

is no overlap. A visualization of the $_{\mathscr{B}}(xz)$ plane illustrating the configurations of the airfoils centerline at two designated instants: at $t = 4.19$ s with the structures in contact, and at $t = 4.77$ s with the structures separated, are presented in Figs. 10c and 10b, respectively.

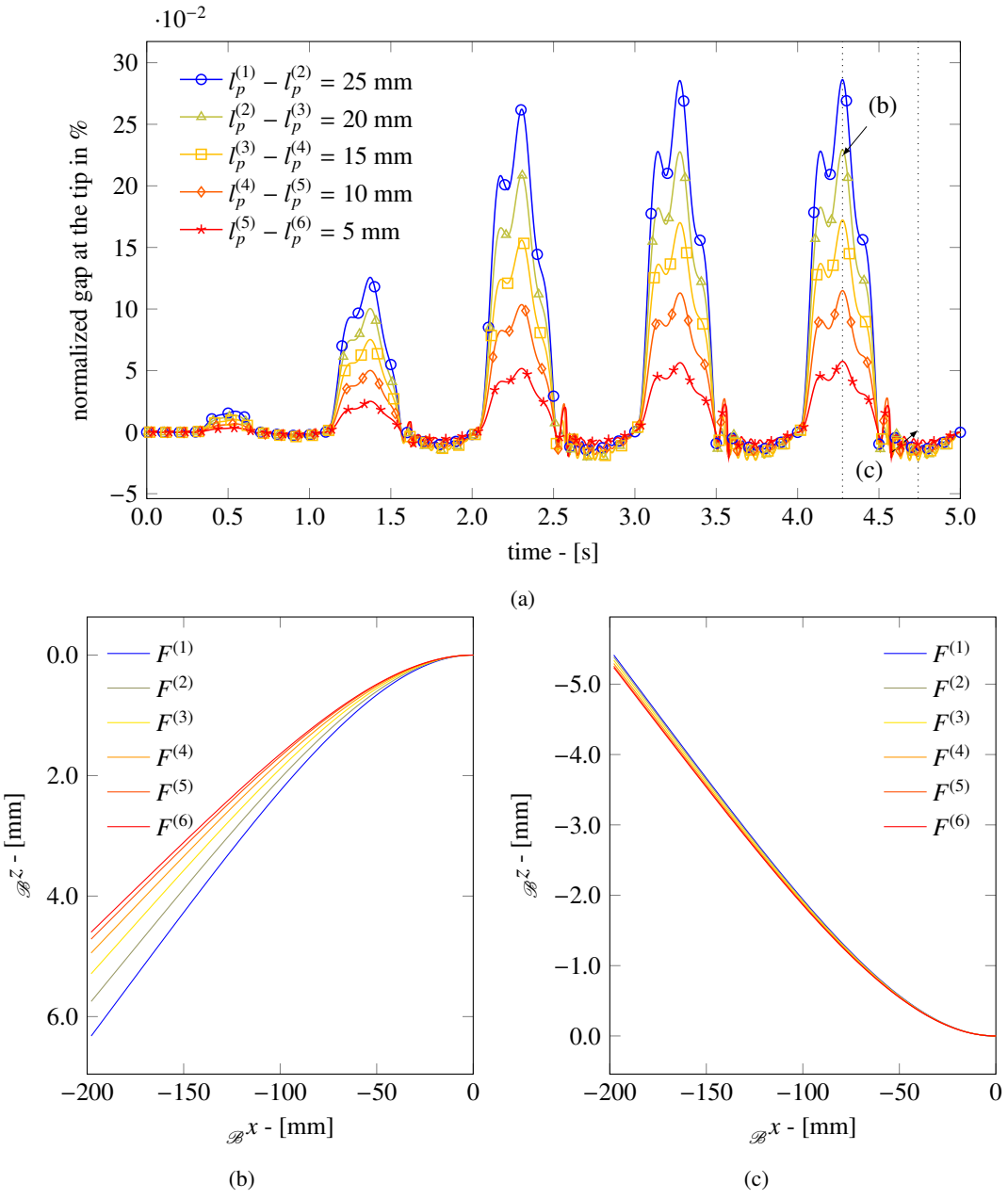


Figure 10: Simulation of the 6 airfoils wing with non-uniform distance undergoing a sinusoidal flapping motion with amplitude $a_F = 30°$ at a frequency of 1 Hz. Illustration of the centerline of each airfoil at (b) $t = 4.276$ s with the airfoils separated and (c) $t = 4.741$ s in contact.

An additional consideration is that the airfoils were assumed perpendicular to the rigid wing structure. In some bioinspired feathered wing designs, the airfoils are clamped at an angle that gradually changes from perpendicular to parallel with the rigid wing [7, 1, 18]. This configuration increases the complexity of the contact search procedure, since

instead of assuming a contact line in advance, the arbitrary geometry of the overlap region requires a parameterization dependent on the angle that each airfoil makes with the wing structure.

5 CONCLUSIONS

The feathered wing is an evolutionary trait exclusive to the bird class perfected during millions of years through natural selection. This design shows interesting dynamic effects such as the separation of the wing feathers during the flapping motion, which creates alternative channels for the air to flow through. On the other hand, the overlap between feathers constrains the direction of this separation such that forces acting from below the wing surface result in an impervious surface for the air.

In this article, a numerical model is developed to investigate the dynamics of a bioinspired flapping wing model composed of multiple airfoils positioned along a rigid wing base with an overlap similar to the disposition of the feathers in a bird's wing. The kinematic parameters of the system are presented and compared with its natural counterpart. The structure of each airfoil is modeled using ANCF beam elements, with its defining terms described. Moreover, the constraint equations responsible for imposing the flapping motion are formulated in terms of the nodal coordinates of the ANCF beam element to obtain an index-3 DAE system as a model for this multi-airfoil wing design.

A line-to-line contact formulation is described to model the overlap region by presenting the contact-search kinematics using an unilateral closest point projection and a penalty formulation model to consider the forces on the contact line. These contact forces are defined in terms of the nodal coordinates alongside their Jacobian matrix to integrate the equation of motion in time using the generalized-α algorithm.

A convergence analysis is presented to assess the number of elements of the ANCF mesh. The equation of motion is solved considering different contact parameters to discuss its effect on the dynamic response. A zero contact stiffness represents the case where the structures deform, such as when they are isolated, and in this setting, the time variation of the nodal coordinates has a predominant waveform at the flapping frequency. When the contact stiffness is increased, the penetration is opposed by the contact force on the overlapping region, which decreases as the contact stiffness is increased. After the structure separates, it is possible to distinguish additional waveforms occurring in each structure at a frequency associated with its structural frequency.

Two models with $n_F = 6$ airfoils are presented, and the effect of the spacing is discussed. It is shown that a uniform distance between airfoils results in gaps with approximately the

same magnitude between each pair. A non-uniform spacing results in gaps that increase with the separation distance between airfoils. The clamping distance between airfoils is a design parameter that is fixed once the vehicle is built. However, real feathers are clamped in a compliant fashion and coupled with elastic elements such that with one biomechanical input, they simultaneously morph the wing shape and, in consequence, this separation is changed [5, 28].

Further investigations have to be carried out to accurately identify the parameters and verify the accuracy of this overlapping airfoil model by measuring and comparing the deformation of each structure during the flapping cycle with experimental results. After a calibration, the model is intended to be used as a reference for future investigation involving different wing designs and operational flapping patterns, which requires the search of a large set of parameters. Moreover, since the ANCF model is computationally expensive to solve, an interesting approach for future investigation is to compare the results obtained by reduced-order models. Additionally, an aerodynamic model has to be coupled to this structural model in a multidisciplinary investigation to evaluate the influence of the aerodynamic forces and quantify the advantages of the airfoil separation in this multi-airfoil wing design.

6 ACKNOWLEDGMENTS

The study was financed, in part, by the São Paulo Research Foundation (FAPESP). Process Number: 2025/09789-3, 2023/04325-3, and 2022/03128-7. The third author thanks the National Council for Scientific and Technological Development (CNPq) for the grant number 308328/2025-6.

REFERENCES

[1] Ajanic, E.; Feroskhan, M.; Mintchev, S.; Noce, F.; Floreano, D.: Bioinspired wing and tail morphing extends drone flight capabilities. Science Robotics, 2020.

[2] Arnold, M.; Brüls, O.: Convergence of the generalized-α scheme for constrained mechanical systems. Multibody System Dynamics, 2007.

[3] Bosten, A.; Cosimo, A.; Linn, J.; Brüls, O.: A mortar formulation for frictionless line-to-line beam contact. Multibody System Dynamics, Vol. 54 pp 31-52, 2021.

[4] Bozorgmehri, B.; Yu, X.; Matikainen, M. K.; Harish, A. B.; Mikkola, A.: A study of contact methods in the application of large deformation dynamics in self-contact beam Nonlinear Dynamics, 2021.

[5] Chang, E.; Matloff, L. Y.; Stowers, A. K.; Lentink, D.: Soft biohybrid morphing wings with feathers underactuated by wrist and finger motion Science Robotics, 2020.

[6] Chung, J.; Hulbert, G. M.: A Time Integration Algorithm for Structural Dynamics With Improved Numerical Dissipation: The Generalized-α Method. Journal of Applied Mechanics, 1993.

[7] Di Luca, M.; Mintchev, S.; Heitz, G.; Noca, F.; Floreano, D.: Bioinspired morphing wings for extended flight envelope and roll control of small drones Interface Focus, 2017.

[8] Ennos, A. R.; Hickson, J. R. E.; Roberts, A.: Function morphology of the vanes of the flight feathers of the pigeon *Columba Livia*. Journal of Experimental Biology, Vol. 198, No. 5, pp. 1219–1228, 1995.

[9] Flores, P.; Ambrósio, J.: On the contact detection for contact-impact analysis in multibody systems. Multibody System Dynamics. 2010.

[10] Flores, P.; Machado, M.; Silva, M. T.; Martins, J. M.: On the continuous contact force models for soft materials in multibody dynamics Multibody System Dynamics, 2011.

[11] Försching, H.; Hennings, H.: Aeroelastic mysteries in avian flight; CEAS Aeronautical Journal, 2012.

[12] García-Vallejo, D.; Mayo, J.; Escalona, J. L.; Domínguez, J.: Efficient Evaluation of the Elastic Forces and the Jacobian in the Absolute Nodal Coordinate Formulation. Nonlinear Dynamics, 2004.

[13] García-Vallejo, Valverde, J. ; Domínguez, J.: An Internal Damping Model for the Absolute Nodal Coordinate Formulation. Nonlinear Dynamics, 2005.

[14] Géradin, M.; Rixen, D. J.:Mechanical Vibrations: theory and application to structural dynamics. Wiley, 2015.

[15] Haddouni, M.; Acary, V.; Garreau, S.; Beley, J.; Brogliato, B.:Comparison of several formulations and integration methods for the resolution of DAEs formulations in event-driven simulation of nonsmooth frictionless multibody dynamics. Multibody System Dynamics, 2017.

[16] Hughes, T. J. R.; Taylor, R. L.; Sackman, J. L.; Curnier, A.: A finite element method for a class of contact-impact problems. Computer Methods in Applied Mechanics and Engineering, 1976.

[17] Iverson, D.; Rahimpour, M.; Lee, W.; Oshkai, P.:Effect of chordwise flexibility on propulsive performance of high inertia oscillating-foils Journal of Fluids and Structures, 2019.

[18] Jeger, S. L.; Wüest, V.; Toumieh, C.; Floreano, D.: Adaptive morphing of wing and tail for stable, resilient, and energy-efficient flight of avian-inspired drones npj Robotics, 2024.

[19] Johnson, K. L.: Contact Mechanics. Cambridge University Press, 1985.

[20] Khulief, Y. A.; Shabana, A. A.: Dynamic Analysis of Constrained System of Rigid and Flexible Bodies With Intermittent Motion. Journal of Mechanisms, Transmissions, and Automation in Design, 1986.

[21] Kim, N.: Introduction to Nonlinear Finite Element Analysis. ISBN 978-1-4419-1745-4, Springer, 2015.

[22] Klaus-Jürgen, B.: Finite element procedures. Prentice Hall, 1996.

[23] Krysko, A. V.; Awrejcewicz, J.; Zhigalov, M. V.; Krysko, V. A.On the contact interaction between two rectangular plates Nonlinear Dynamics, 2016.

[24] Lalanne, M.; Berthier, P.; Johan Der Hagopian: Mechanical Vibrations for Engineers ISBN 0 471 90197 0, John Wiley & Sons Ltd, 1984.

[25] Laursen, T. A.: Computational Contact and Impact Mechanics. Springer, 2002.

[26] Liu, Y.; Zhang, J.; Gao, L.; Zhu, Y.; Liu, B.; Zang, X.; Cai, H.; Zhao, J.: Employing Wing Morphing to Cooperate Aileron Deflection Improves the Rolling Agility of Drones. Wiley, 2023.

[27] Machado, M.; Moreira, P.; Flores, P.; Lankarani, H. M.: Compliant contact force models in multibody dynamics: Evolution of the Hertz contact theory. Mechanism and Machine Theory, 2012.

[28] Matloff, L. Y.; Chang, E.; Feo, T. J.; Jeffries, L.; Stowers, A. K.; Thomson, C.; Lentink, D.: How flight feathers stick together to form a continuous morphing wing Science, 2020.

[29] Meier, C; Popp, A; Wolfgang A. Wall: A Finite Element Approach for the Line-to-Line Contact Interaction of Thin Beams with Arbitrary Orientation. Computer Methods in Applied Mechanics and Engineering, Vol. 308 pp. 377–413, 2016.

[30] Mujires, F. T.; Johansson, L. C.; Bowlin, M. S.; Winter, Y.; Hedenstroön, A.: Comparing Aerodynamic Efficiency in Birds and Bats Suggests Better Flight Performance in Birds PLOS ONE, 2012.

[31] Obrezkov, L.; Bozorgmehri, B; Kouhia, R.; Matikainen, M. K.: Contact formulations for analysis of micropolar media with finite continuum beam elements International Journal of Solids and Structures, 2024.

[32] Oorschot, B. K. van; Choroszucha, R.; Tobalske, B. W.:Passive aeroelastic deflection of avian primary feathers. Bioinspiration & Biomimetics, 2020.

[33] Sim, W.; Lee, B.; Kim, D. J.; Lee, J. A.; Kim, J.; Chung, J.: Vibro-impact analysis of two adjacent cantilever beams Nonlinear Dynamics, 2022.

[34] Sullivan, T. N.; Wang, B.; Espinosa, H. D.; Meyers, M. A.: Extreme lightweight structures: avian feathers and bones. Materials Today, 2017.

[35] Tomec, J.; Jelenić, G.: Analysis of static frictionless beam-to-beam contact using mortar method. Multibody System Dynamics, Vol. 55, No. 3, pp. 293–322, 2022.

[36] Weyler, R.; Oliver, J.; Sain, T.; Cante, J. C.: On the contact domain method: A comparison of penalty and Lagrange multiplier implementations Computer Methods in Applied Mechanics and Engineering, 2012.

[37] Yakoub, R. Y.; Shabana, A. A.: Three Dimensional Absolute Nodal Coordinate Formulation for Beam Elements: Implementation and Applications. Journal of Mechanical Design, 2003.

[38] Yang, W.; Song, B.: Experimental Investigation of Aerodynamics of Feather-Covered Flapping Wing Applied Bionics and Biomechanics, 2017.